

STAR FORMATION IN INTERMEDIATE REDSHIFT $0.2 < Z < 0.7$ BRIGHTEST CLUSTER GALAXIES

KEVIN C. COOKE¹, CHRISTOPHER P. O'DEA^{1,2}, STEFI A. BAUM^{1,2}, GRANT R. TREMBLAY³, ISABELLA G. COX¹, AND
 MICHAEL D. GLADDERS⁴

¹School of Physics and Astronomy, Rochester Institute of Technology, Rochester, NY 14623, USA; kcc7952@rit.edu

²Department of Physics and Astronomy, University of Manitoba, Winnipeg, MB R3T 2N2, Canada

³Department of Astronomy and Physics, Yale University, New Haven, CT 06511, USA

⁴Department of Astronomy and Astrophysics and Kavli Institute for Cosmological Physics,
 University of Chicago, 5640 South Ellis Avenue, Chicago, IL 60637, USA

The Astrophysical Journal, 833:224 (10pp), 2016 December 20

ABSTRACT

We present a multi-wavelength photometric and spectroscopic study of 42 Brightest Cluster Galaxies (BCGs) in two samples of galaxy clusters chosen for a gravitational lensing study. The study's initial sample combines 25 BCGs from the Cluster Lensing and Supernova Survey with Hubble (CLASH) sample and 37 BCGs from the Sloan Giant Arcs Survey (SGAS) with a total redshift range of $0.2 < z < 0.7$. Using archival *GALEX*, *Hubble Space Telescope*, *Wide-Field Infrared Survey Explorer*, *Herschel*, and Very Large Array data we determine the BCGs' stellar mass, radio power, and star formation rates. The radio power is higher than expected if due to star formation, consistent with the BCGs being active galactic nucleus (AGN)-powered radio sources. This suggests that the AGN and star formation are both fueled by cold gas in the host galaxy. The specific star formation rate (sSFR) is low and constant with redshift. The mean sSFR is $9.42 \times 10^{-12} \text{ yr}^{-1}$, which corresponds to a mass doubling time of 105 billion years. These findings are consistent with models for hierarchical formation of BCGs, which suggest that star formation is no longer a significant channel for galaxy growth for $z \leq 1$. Instead, stellar growth (of the order of a factor of at least two) during this period is expected to occur mainly via minor dry mergers.

Keywords: galaxies: clusters, galaxies: elliptical and lenticular, cD, galaxies: clusters: intracluster medium, galaxies: star formation

1. INTRODUCTION

The most massive and luminous galaxies observed are the Brightest Cluster Galaxies (BCGs). They are typically located in the centers of galaxy clusters, indicating a relaxed position in the cluster potential. Their formation models are environmentally dependent, and distinct from typical elliptical galaxies (e.g., Lin & Mohr 2004; Brough et al. 2005; De Lucia & Blaizot 2007). BCGs are also more likely to host active galactic nuclei (AGNs) than other galaxies of the same stellar mass (e.g., Best et al. 2007; Von Der Linden et al. 2007). This indicates that these objects play a pivotal role in quenching cooling flows and star formation in clusters (McNamara & Nulsen 2007, 2012; Fabian 2012). BCGs have been recently shown to lie off the standard scaling relations of early-type galaxies (e.g., Bernardi et al. 2007; Lauer et al. 2007; Von Der Linden et al. 2007; Bernardi 2009). In particular, they show excess luminosity (or stellar mass) above the prediction of the standard Faber–Jackson relation at high galaxy masses (e.g., Lauer et al. 2014).

Stellar population synthesis models suggest that the bulk of star formation in most massive galaxies took place prior to $z \sim 2$ (e.g., Thomas et al. 2005; Treu et al. 2005; Jimenez et al. 2007). Semi-analytical models also suggest that the stars that make up most of the BCG mass are formed very early on (80% by $z \sim 3$; De Lucia et al. 2006, De Lucia & Blaizot 2007). Only after most stars have been formed does the final galaxy assembly take place via merging. The final galaxy mergers in BCG formation ($z < 1$) are expected to be predominantly dissipationless (or dry, i.e., not involving large

amounts of gas; Khochfar & Burkert 2003, De Lucia & Blaizot 2007, Vulcani et al. 2016).

Thus, a strong prediction of the hierarchical galaxy formation models is that at $z < 1$, star formation should make a only minor contribution to the growth of the stellar mass of BCGs. This has been confirmed at low redshift (e.g., Pipino et al. 2009; Donahue et al. 2010; Wang et al. 2010; Liu et al. 2012; Fraser-McKelvie et al. 2014). The vast majority of the BCGs studied previously have been at $z < 0.3$. McDonald et al. (2016) explored a much larger redshift range from $0.25 < z < 1.25$ and found that BCG star formation transitions from a disturbed cluster paradigm at $z > 0.6$ to a cool-core paradigm at $z = 0$. They also find that at $z \sim 0.4$, 20% of BCGs are forming stars at $> 10 M_{\odot} \text{ yr}^{-1}$. To investigate this transition era, we present a study of star formation in two samples of BCGs (in clusters chosen for the study of gravitational lensing) that lie in the range $0.2 < z < 0.7$.

The outline for the paper is as follows. In Section 2, we discuss the sample selection criteria. In Section 3, we discuss the archival data used in the analysis. In Section 4, we discuss how we estimated the star formation rates, stellar masses, and radio power for the BCGs. In Section 5, we discuss the implications for formation models of BCGs. In Section 6, we give our conclusions.

This paper uses the current Λ CDM cold dark matter (Λ CDM) parameters of $H_0 = 70 \text{ Mpc}^{-1} \text{ km s}^{-1}$, $\Omega_M = 0.3$, and $\Omega_{vac} = 0.7$.

2. SAMPLE SELECTION

We studied all the BCGs from two samples of clusters selected for studies of gravitational lensing - the Sloan Giant Arcs Survey (SGAS: Bayliss et al. 2011) and the Cluster Lensing and Supernova Survey with Hubble (CLASH: Postman et al. 2012). The two samples cover a redshift range $0.2 < z < 0.7$. The clusters were not chosen on the basis of the star formation properties of the BCGs. The coordinates, redshifts, and modeled stellar mass of this BCG sample are described in Table 1 and their star formation rates from UV and optical methods are listed in Table 2.

The 37 clusters in SGAS includes clusters selected from two different surveys and methods (Oguri et al. 2012). The first method is visual inspection of SDSS photometry of BCGs for strongly lensing systems (Bayliss et al. 2011, M. D. Gladders et al., in preparation). The second method is a “blind study” in which SDSS g -band images of the 240 most massive clusters in the SDSS are selected based on lensing strength (Hennawi et al. 2008).

The selection criteria for the 25 CLASH clusters are discussed in detail by Postman et al. (2012). They selected 20 massive clusters from X-ray-based compilations of dynamically relaxed systems. Of these 20 clusters, 16 were taken from the Allen et al. (2008) compilation of massive relaxed clusters. An additional five clusters were added due to their exceptional strength as gravitational lenses (Einstein radii $> 35''$). The star formation properties of the CLASH BCGs are discussed independently (Donahue et al. 2015; Fogarty et al. 2015) with results that are in agreement with those reported here.

3. ARCHIVAL DATA

3.1. GALEX Observations

In order to measure the population of young, massive stars in BCGs we obtained archival far-UV (FUV) and near-UV (NUV) band total pipeline photometric magnitudes from the GR6/GR7 release of the *Galaxy Evolution Explorer* (GALEX; Martin et al. 2005). GALEX photometry is taken using a 50 cm diameter Ritchey-Chretien telescope with a 1.2° circular field of view. To correct for galactic extinction, $E(B - V)$ values are retrieved from the GALEXview webpage for each of the target locations observed by GALEX (Morrissey et al. 2007). Internal extinction is not corrected for due to $H\alpha$ being redshifted out of SDSS spectral coverage for much of our sample. This prevents the use of the Balmer decrement to approximate internal dust levels across our entire sample. Our sample K-corrections are not calculated in the UV due to the presence of limits in the SDSS observations necessary for k-correction calculation. Previous CLASH UV findings (Donahue et al. 2015) have found k-corrections are less than 10% and do not significantly effect results. Archival data is a mixture of All Sky and Medium Imaging with depths of 20.5 and 23.5 m_{AB} respectively. For the farthest and least sensitive AIS case, MACS1149.6+2223, this corresponds to a SFR upper limit of $4.84 M_\odot \text{ yr}^{-1}$. Even in the worst-case scenario, this is still sensitive enough to detect examples of exceptionally high star formation and we only use these limits in cases with no optical emission line detections.

The UV contribution from an old stellar population, called the “UV-upturn” (O’Connell 1999), can be addressed through modeling of the spectra of other ellipti-

cals in the BCG’s cluster (e.g. Hicks et al. 2010; Fogarty et al. 2015). In order to predict the old stellar UV contribution in a given target, we acquired a UV-optical-near-infrared (NIR) spectrum previously constructed using satellite ellipticals in the CLASH sample clusters (Fogarty et al. 2015, and K. Fogarty 2016, private communication). These templates are composites of quiescent populations and do not include ongoing star formation components. To approximate the UV from old stars, Fogarty et al. (2015) scaled their template to the available UV-Optical-NIR observations of the CLASH BCGs and derived a modeled J-band flux. The correlation between J-band and NUV for old stellar populations in BCGs prescribed in Table 5 of Hicks et al. (2010) was then used to generate an old stellar NUV flux. We performed our SED scaling using the I-band from SDSS. The Z-band was not used due to the more common occurrence of upper limits.

3.2. Sloan Digital Sky Survey Observations (SDSS)

In order to measure the optical SED of the BCGs, we use the Catalog Archive Server Jobs System (CASJOBS; Li & Thakar 2008) to obtain archival *ugriz* Petrosian magnitudes (Petrosian 1976) from the SDSS (Gunn et al. 2006). SDSS reports that the pipeline Petrosian magnitudes reliably include 80% of a galaxy’s light independent of distance (Blanton et al. 2001). We use Data Release 12 (DR12) results (Alam et al. 2015). If the observed Petrosian magnitudes are lower than SDSS *ugriz* limiting magnitudes [22.0, 22.2, 22.2, 21.3, 20.5], respectively, the galaxy is considered a non-detection and the Petrosian magnitude is used as a limit (Ahn et al. 2012). We take extinction magnitudes from the photoObj SDSS tables to correct Milky Way foreground extinction. Foreground extinction magnitudes assume a Milky Way Galaxy extinction map from (Schlafly & Finkbeiner 2011) assuming a galactic reddening of $R_v = 3.1$.

To measure the emission line features of the BCGs, we use archival spectral measurements and errors from SDSS DR12. SDSS multi-object spectroscopy is taken using fibers that subtend $3''$ on the sky, large enough to include the majority of a given BCG. The effects of this fixed aperture size, and its relation to the other apertures used for the photometry, are discussed in Section 4. Emission and absorption features in SDSS spectra are fit and stored in the galspecLine view in the publicly available Sky Server database of SDSS as a feature of the standard pipeline reduction of DR12. Foreground extinction was corrected for using the Milky Way extinctions calculated above.

3.3. WISE Observations

The *Wide-field Infrared Survey Explorer* (WISE) is a NASA space telescope (Wright et al. 2010) designed to perform an all sky survey using four bands. To constrain the old stellar population during SED fitting, we retrieved WISE profile fit 3.4, 4.6, 12 and 22 μm (W1, W2, W3, and W4) magnitudes from the NASA/IPAC Infrared Science Archive AllWISE Source Catalog (Cutri & et al. 2013). The AllWISE catalog co-added exposures from the cryogenic and NEOWISE phases, resulting in 5σ flux detections at 16.9, 16.0, 11.5, and 8.0 m_{Vega} for W1, W2, W3, and W4, respectively. Magnitudes are

reported with photometric quality flags. We treat data with flags U (95% confidence upper limit) and C ($2 < \text{SNR} < 3$) as upper limits, and trust the stronger A ($\text{SNR} > 10$) and B ($3 < \text{SNR} < 10$) flags as detections. Extinction in the infrared is negligible and is not corrected for in our work.

3.4. *Herschel* Observations

To better characterize absorbed and re-emitted starlight from dust, we obtained archival data from the *Herschel Space Observatory* (*Herschel*) – a European Space Agency (ESA) built far infrared/submillimeter telescope launched in 2009 (Pilbratt et al. 2010). Archival Photoconductor Array Camera and Spectrometer (PACS) green band ($100\ \mu\text{m}$), and red band ($160\ \mu\text{m}$) photometry were acquired through the *Herschel* Science Archive. A subset of CLASH galaxies were observed by the *Herschel* Lensing Survey (Egami et al. 2010) with flux limit of 2.4 mJy ($100\ \mu\text{m}$) and 4.7 mJy ($160\ \mu\text{m}$). One SGAS target was observed by Rhoads et al. (2014); SDSSJ0915+3826 to limits of 5.2 mJy ($100\ \mu\text{m}$) and 9.9 mJy ($160\ \mu\text{m}$). Another was observed by Saintonge et al. (2013); SDSSJ1343+4155 to limits of 4.42 mJy ($70\ \mu\text{m}$) 9.9 mJy ($160\ \mu\text{m}$).

To guarantee up-to-date calibrations for our faint sources, we re-reduced this sample’s *Herschel* PACS photometry with *Herschel* Interactive Programming Environment (HIPE) from the raw level 1 maps to the science quality level 2.5 using the MadMap pipeline (Cantalupo et al. 2010). This step is done in order to examine images with the latest *Herschel* PACS calibration files. Level 1 maps was retrieved from the *Herschel* Science Archive (HSA) with PACS calibration version PACS_CAL_69.0. MadMap removes the most common noise source in *Herschel* PACS images, the $1/f$ noise. $1/f$ noise is the randomized photon noise over time the detector observes along with the target photons. Once the level 2.5 maps are produced from HIPE’s reduction process, the task `sourceExtractor` was used to measure individual object fluxes and errors while correcting for sky background. Afterward, we ran the `sourceExtractor` task built into HIPE to detect objects with a S/N threshold of 3 using a gaussian with band-specific FWHMs of $10.5''$, $6.67''$, and $5.4''$ for red ($160\ \mu\text{m}$), green ($100\ \mu\text{m}$), and blue ($70\ \mu\text{m}$) channels, respectively (PACS Handbook).

3.5. *Very Large Array* (VLA) Observations

In order to quantify the activity of the supermassive black hole in each BCG, Karl G. Jansky VLA (Thompson et al. 1980) radio observations of observer-frame 1.4 GHz flux are taken from the 2014 version of the NRAO VLA Sky Survey (NVSS; Condon et al. 1998) and the Faint Images of the Radio Sky at Twenty-Centimeters (FIRST) Survey Catalog (Helfand et al. 2015). NVSS is designed to observe 1.4 GHz emission at a low resolution of $45''$ across the entire sky north of $\delta = -40^\circ$. FIRST is a large-scale ($>10,000\ \text{deg}^2$) survey that observed the radio sky at a resolution of $5''$ from 1993 to 2011 (Helfand et al. 2015).

For objects with observations in both the NVSS and FIRST archival catalogs, preference is given to FIRST observations that have a better angular resolution as well as an rms of 0.15 mJy versus NVSS’s rms of 0.45 mJy

per beam. Nine BCGs observed by NVSS and FIRST do not have fully reduced photometry available in the published catalogs. We used the Common Astronomy Software Applications (McMullin et al. 2007) package to perform background subtraction and record the target radio flux or the upper limit if there is no visible source in the image. Observations were k-corrected and extrapolated to target-frame 1.4 GHz using a spectral index of 0.75, common for BCGs (Hlavacek-Larrondo et al. 2013; Giacintucci et al. 2014).

4. ANALYSIS

BCG luminosity and stellar mass estimates were derived from the publicly available galaxy SED fitting software MAGPHYS (da Cunha et al. 2008). MAGPHYS fits the SED of each galaxy using two components; UV to optical and NIR to FIR. The fitting is done self-consistently, modeling the FIR flux considering the star formation fitted to the UV and optical. Rather than the default Bruzual (2007) models, we use the Bruzual & Charlot (2003) stellar population models found to successfully model BCGs in the past (e.g. Lidman et al. 2012). The infrared models include PAH, cold (15–25 K), warm (30–60 K), and hot (130–250 K) dust components. MAGPHYS fitted values used here include the total stellar mass. Flux reduction due to cosmological expansion is accounted for by MAGPHYS before the fitting process using redshifts reported by Postman et al. (2012) for CLASH targets and Alam et al. (2015) for SDSS targets.

Five of the SGAS sample BCGs lacked SDSS photometric or spectroscopic redshifts at the time of this work and could not be accurately modeled: SDSSJ0333-0651, SDSSJ1420+3955, SDSSJ1522+2535, SDSSJ1621+0607, and SDSSJ2243-0935. Additionally, SDSSJ0915+3826 and SDSSJ0928+2031 both had failed fits with infinite χ^2 . This is believed to have occurred due to a combination of lack of NIR data as well as having the majority of its SDSS fluxes as limits. These two are removed from the following statistics and plots. An additional 13 targets had no SDSS spectra or GALEX photometry within $10''$, resulting in the final sample of 42 BCGs.

Total star formation rate estimates from MAGPHYS are not used due to the poor infrared coverage of the SGAS sample. The fitting procedure systematically overestimates the far infrared luminosity in the SGAS sample due to lack of constraints. This high estimated infrared luminosity corresponds to total star formation rates much higher than that which is consistent with the lack of dust and substructure seen in HST photometry. However, the stellar mass estimates from MAGPHYS use the well-characterized optical-NIR continuum and are used further in this study. For this study’s results, we use the Kennicutt (1998) calibrations for optical emission line SFR estimates. We use SDSS $H\alpha$ fluxes where possible, followed by $[\text{O II}]$ when $H\alpha$ was redshifted out of the SDSS coverage. GALEX NUV photometry was retrieved in the case where SDSS spectra are not available and we approximate the SFR using the Kennicutt (1998) UV continuum calibration.

The SGAS subsample SFRs are predominantly approximated using $H\alpha$ and $[\text{O II}]$ emission measured through the $3''$ diameter fibers of the SDSS multi-object spectrograph. CLASH targets not observed by SDSS have

SFRs approximated through GALEX NUV flux measured through elliptical Kron apertures in which the radius is 2.5 times the first moment of the target’s radial profile. The Kron radii used for targets in our sample range from 3” to 5” in radius. CLASH SFRs are likely to be more accurate than SDSS fibers, which may miss star-forming knots in a given galaxy. One recent example is Tremblay et al. (2014) study of star formation filaments in a merging system of two massive ellipticals. Slit spectroscopy using the ALFOSC spectrograph on the Nordic Optical Telescope found 1.7 times the SDSS H α flux reported in SDSS Data Release 9. To correct for this effect would require a priori knowledge of the distribution, shape, and intensity of star-forming knots in all galaxies in our sample, so we leave the SDSS fluxes as reported by the pipeline. Thus, the SGAS SFRs estimated using SDSS spectra will likely be lower limits to the true SFR.

Additionally, as a sanity check for our MAGPHYS stellar mass results, we compare with previous estimates of the CLASH subsample from Burke et al. (2015) and we are within 30%. For example, RXJ1532+30’s stellar mass is estimated by Burke et al. (2015) to be $2.20 \pm 0.05 \times 10^{11} M_{\odot}$ while we estimate $2.88 \pm 0.06 \times 10^{11} M_{\odot}$. Their methodology uses magnitudes from the Postman et al. (2012) observations fit to a spectral energy distribution produced by Bruzual & Charlot (2003) solar metallicity models. The combined CLASH-SGAS sample has a mean stellar mass of $7.52 \times 10^{11} M_{\odot}$ and standard deviation of $6.22 \times 10^{11} M_{\odot}$.

5. DISCUSSION

5.1. Dependencies With Mass

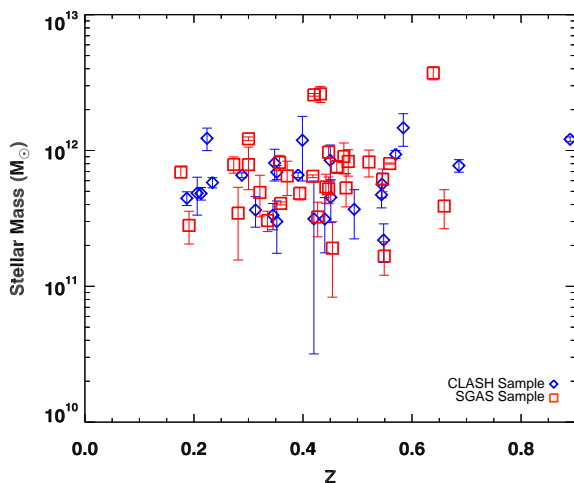


Figure 1. BCG stellar mass versus redshift of both samples as fit by MAGPHYS. Red squares are SGAS sample galaxies. Blue diamonds are CLASH sample galaxies. Error bars are 1σ .

In Figure 1 we show the total stellar masses (estimated as described in § 4) as a function of redshift. There is no trend of stellar mass with redshift over the range $z = 0.2 - 0.7$. We confirmed that the masses of the CLASH and SGAS samples are statistically similar using a Kolmogorov–Smirnov test implemented using IDL’s

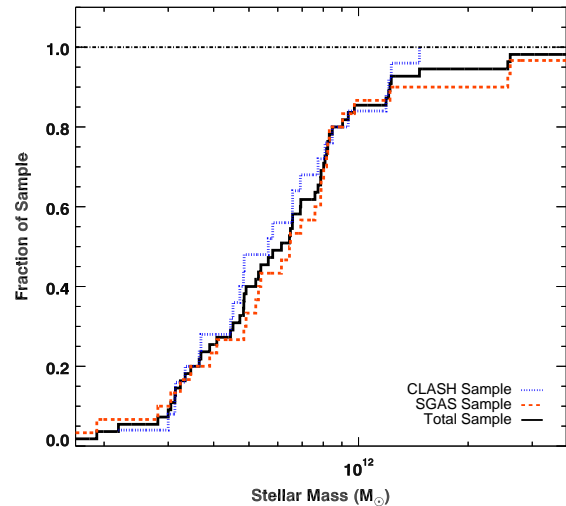


Figure 2. Cumulative histogram of stellar masses calculated for CLASH (dotted blue line), SGAS (dashed red line), and the combined sample (solid black line).

kstwo procedure on both samples. The probability the subsamples are identical is 0.75, with a maximum difference of 1.5% between subsample distribution functions as seen in Figure 2.

In Figure 3 we examine the importance of star formation activity to a galaxy’s evolution by comparing the star formation rate with the total stellar mass. Previous results show that at redshifts $0 < z < 2$, star-forming galaxies in general show a correlation between stellar mass and star formation rate, which has been called a Star Formation Main Sequence (SFMS; e.g. Brinchmann et al. 2004; Daddi et al. 2007; Elbaz et al. 2007; Noeske et al. 2007; Santini et al. 2009; Lara-López et al. 2010; Zahid et al. 2013; Vaddi et al. 2016). No SFMS trend is seen in our sample. This corroborates previous results by Lee et al. (2015) in which the SFMS is nearly flat (or absent) above $10^{11} M_{\odot}$.

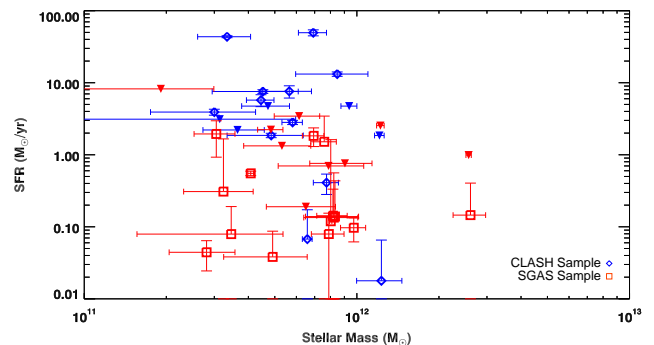


Figure 3. Star formation rate versus stellar mass of both samples as fit by MAGPHYS. Red squares are SGAS sample galaxies. Blue diamonds are CLASH sample galaxies. Error bars are 1σ . Downward-facing triangles are upper limits. Missing lower limit bars are an artifact of plotting large errors on a log scale.

5.2. Radio Behavior

The observed radio powers and upper limits of the BCGs (Figure 4) are one to two orders of magnitude above the radio powers expected if due solely to star formation estimated following Condon (1992). This suggests that the radio emission is being powered by the AGNs in these BCGs. This is consistent with previous evidence that BCGs are often radio loud. The fraction of galaxies that are radio loud increases with galaxy mass (e.g., Auriemma et al. 1977; Dressel 1981; Ledlow & Owen 1996; Best et al. 2005; Von Der Linden et al. 2007). In addition, the average (and maximum) observed radio power increases with galaxy mass (e.g., Brown et al. 2011; Vaddi et al. 2016). This suggests that the source of fuel for AGN activity increases with galaxy mass; though radio power and mechanical power are not just a simple function of the accretion rate (e.g., McNamara & Nulsen 2007, 2012; Best & Heckman 2012). Nevertheless, this is consistent with cold gas being the source of fuel for both the AGN and star formation activity. Cold gas has been suggested as the fuel for AGN activity (e.g., Pizzolato & Soker 2005; Gaspari et al. 2013, 2015; Li & Bryan 2014). There is evidence for infalling molecular gas in some BCGs, such as in A2597 (Tremblay et al. 2016).

BCGs are more often found to be radio loud than non-BCG galaxies of the same mass (Best et al. 2007; Von Der Linden et al. 2007). This suggests that the BCGs have an additional source of gas that is not present in non-BCG galaxies of the same mass. Alternately, BCGs could have larger mass black holes than non-BCG galaxies of the same stellar mass (e.g., Hlavacek-Larrondo et al. 2012). The additional source of gas in the BCGs is likely to be cooling from the hot ICM in cool-core clusters (e.g., Fabian 1994; Best et al. 2007; Sun 2009). The additional source of gas in the cool-core BCGs results in higher star formation than in the non-cool-core BCGs (see §5.3).

We find the range of BCG radio powers ($L_{1.4\text{GHz}} \approx 10^{24-25} \text{ W Hz}^{-1}$) lie in the FR II (Fanaroff & Riley 1974; Bridle 1984) regime. These radio powers are sufficient to provide significant mechanical mode feedback to the environment, quenching star formation in the BCG (McNamara & Nulsen 2007, 2012; Fabian 2012). A radio power of $10^{25} \text{ W Hz}^{-1}$ corresponds to a νP_ν Luminosity of 10^{34} W . Assuming a 1% efficiency of conversion of jet power to radio power (Eilek & Shore 1989; Cavagnolo et al. 2010; Daly et al. 2012) and 10% conversion of rest mass energy to jet power gives a mass accretion rate of $\sim 10^{-4} \text{ M}_\odot \text{ yr}^{-1}$, which is small compared to the SFR.

5.3. Dependencies with Redshift

We plot star formation rates versus redshift in Figure 5. The estimated star formation rates show no trend with redshift over the range $z = 0.2 - 0.6$. The SFR rates vary mostly between about 0.1 and $10 \text{ M}_\odot \text{ yr}^{-1}$. Examples of CLASH BCGs with high star formation rates are discussed in Fogarty et al. (2015).

We show the specific star formation rate (sSFR; star formation rate per unit stellar mass, e.g., Brinchmann et al. 2004) in Figure 6. There is no trend in sSFR with redshift over the range $z = 0.2 - 0.6$. There is slight difference in the sSFRs of the SGAS and CLASH samples. For the combined MAGPHYS modeled data set of 17 CLASH BCGs and 24 SGAS BCGs, IDL's `twosamp` task found that CLASH and SGAS have a probability

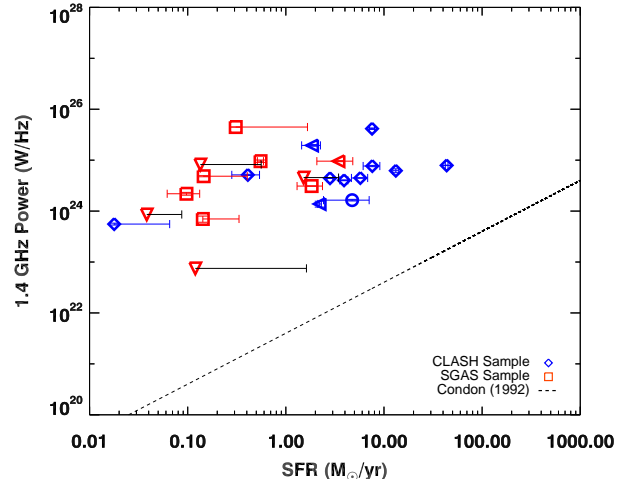


Figure 4. FIRST and NVSS 1.4 GHz rest-frame emission assuming $\alpha = 0.75$. The representative radio emission due to a star-formation-dominated scenario is plotted with the dashed line (Condon 1992). Upper limits are the downward-facing triangles and from CASA-derived background-corrected photometry on target locations. Red squares are SGAS sample galaxies. Blue diamonds are CLASH sample galaxies. Error bars are 1σ . Downward-facing and leftward-facing triangles are upper limits for radio power and SFR, respectively. Open circles indicate that both quantities are upper limits. Missing lower limit bars are an artifact of plotting large errors on a log scale.

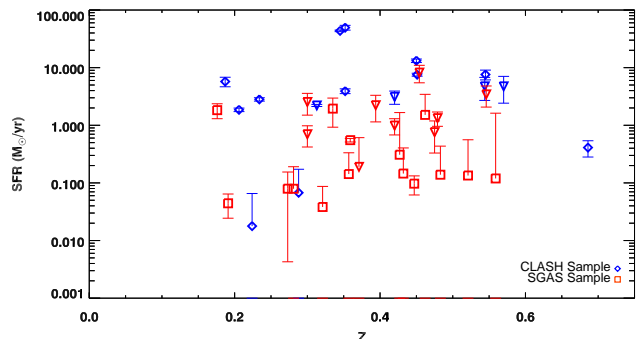


Figure 5. Star formation rate versus redshift of both samples. Red squares are SGAS sample galaxies. Blue diamonds are CLASH sample galaxies. Error bars are 1σ . Downward-facing triangles are upper limits. Missing lower limit bars are an artifact of plotting large errors on a log scale.

of 49% of being the same distribution. This difference is likely due to the much smaller apertures used for measuring the $\text{H}\alpha$ flux used in the SFR determinations of the SGAS sample.

The mean sSFR is $9.42 \times 10^{-12} \text{ yr}^{-1}$ in our study, which corresponds to a mass doubling time of 105 billion years. Thus, the low SFR and sSFR suggest that galaxy growth via star formation in BCGs is minimal by $z \sim 0.7$ consistent with other studies of star formation in lower redshift BCGs (e.g. Pipino et al. 2009; Donahue et al. 2010; Wang et al. 2010; Liu et al. 2012; Fraser-McKelvie et al. 2014) as shown in Figure 7. The outlier BCGs, which have higher than average star formation, tend to be in cool-core clusters (e.g. Crawford et al. 1999; Edwards et al. 2007; O’Dea et al. 2008, 2010; Pipino et al. 2009; Donahue et al. 2010; Hicks et al. 2010; Wang et al.

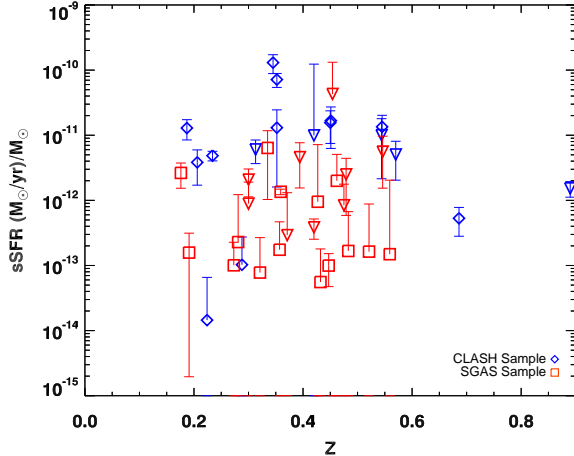


Figure 6. Specific star formation rate (sSFR) versus redshift of both samples. Red squares are SGAS sample galaxies. Blue diamonds are CLASH sample galaxies. Error bars are 1σ . Downward-facing triangles are upper limits. Missing lower limit bars are an artifact of plotting large errors on a log scale.

2010; Pipino et al. 2011; Liu et al. 2012; Mittal et al. 2015; Tremblay et al. 2015; Donahue et al. 2015; Fogarty et al. 2015).

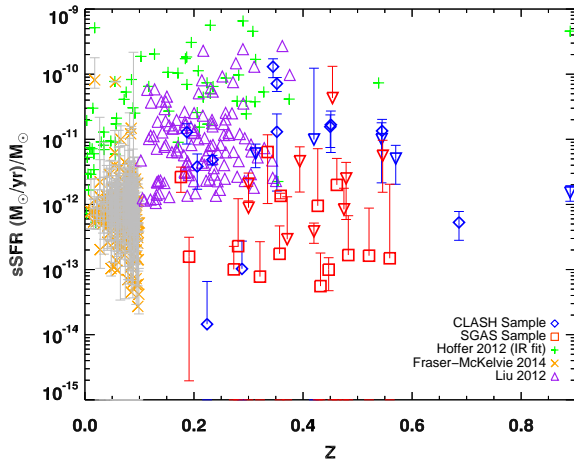


Figure 7. Specific star formation rate (sSFR) versus redshift, which includes published values for lower redshift samples. Red squares are SGAS sample galaxies. Blue diamonds are CLASH sample galaxies. Error bars are 1σ . Downward-facing triangles are upper limits. Missing lower limit bars are an artifact of plotting large errors on a log scale.

5.4. Growth by Mergers?

Growth of the mass of BCGs by mechanisms that do not involve star formation (e.g., dry mergers) is not ruled out by this study of star formation. However, the lack of a redshift dependence on the BCG stellar mass (Figure 1) rules out a *large* gain in stellar mass over the redshift range $z = 0.3 - 0.6$ but probably allows a factor-of-two change in stellar mass over the redshift range $0 < z < 1$. The previous observational work is somewhat inconsistent. Figure 8 shows no clear trends in stellar mass with redshift, but the different samples have identified BCGs

with different mass ranges. Whiley et al. (2008) find no evidence for factor-of-two growth in BCG mass since $z \sim 1$. Collins et al. (2009) find no difference in mass between BCGs at $z \sim 1.3$ and $z \sim 0$. Stott et al. (2011) show that BCGs have evolved little in size since $z \sim 1$. Inagaki et al. (2015) find no evidence for more than a few percent mass growth between $z \sim 0.4$ and $z \sim 0.2$. In contrast, other work has found evidence for the expected increase in BCG stellar mass by about a factor of two between $z \sim 1$ and $z \sim 0$ (e.g., Lidman et al. 2012; Burke & Collins 2013; Lin et al. 2013; Ascaso et al. 2014; Shankar et al. 2015). Our specific sSFR results (Figure 7) corroborate McDonald et al. (2016) results, which BCGs are evolving slower than other galaxies in cluster environments. This would point to an alternate fuel source to keep BCGs mildly active when their satellites have been quenched. The differences between the conclusions of these studies may be due to how the samples were defined and the effects of progenitor bias (e.g., van Dokkum & Franx 1996; Hopkins et al. 2009; Saglia et al. 2010; Carollo et al. 2013; Shankar et al. 2015).

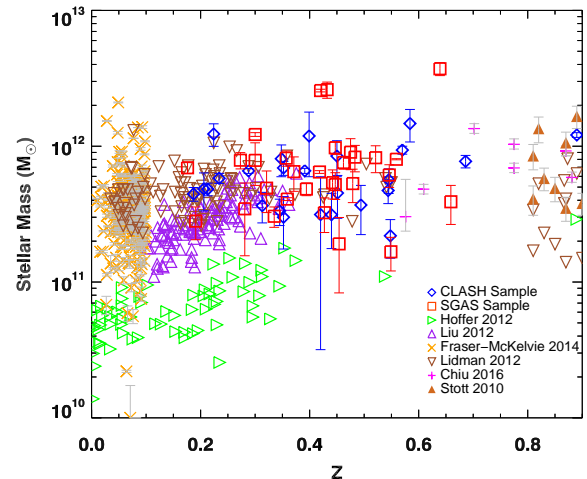


Figure 8. BCG stellar mass vs. redshift from different published samples of BCGs. Red squares are SGAS sample galaxies. Blue diamonds are CLASH sample galaxies. Error bars are 1σ . Downward-facing triangles are upper limits. Missing lower limit bars are an artifact of plotting large errors on a log scale.

For the subset of star-forming BCGs of the CLASH subsample, the fuel for the star formation is attributed to gas condensing out of a cool core (Donahue et al. 2015; Fogarty et al. 2015) which is consistent with the clusters having been X-ray selected. In the SGAS BCGs, X-ray evidence for cool cores is not yet available. We tentatively attribute the source of the fuel for star formation to a major merger in SDSSJ1336-0331 (Figure 9) and SDSSJ1531-3414 (Tremblay et al. 2014).

6. CONCLUSIONS

We present multi-wavelength estimates of star formation rates, and estimates of radio power and stellar mass for BCGs in two samples of clusters chosen for the study of gravitational lensing - CLASH and SGAS. The redshift range of the BCGs $0.2 < z < 0.7$ spans a large fraction of the range over which models of hierarchical galaxy formation suggest that star formation is no longer a significant

channel for galaxy growth. Instead, stellar growth (of the order of a factor of at least two) during this period is expected to occur mainly via minor dry mergers (e.g., De Lucia & Blaizot 2007).

We find that SFRs and sSFRs are indeed low in BCGs $0.2 < z < 0.7$ (excluding some BCGs in cool-core clusters) consistent with results from samples of lower redshift BCGs (e.g., Pipino et al. 2009; Donahue et al. 2010; Wang et al. 2010; Liu et al. 2012; Fraser-McKelvie et al. 2014). The mean sSFR is $9.42 \times 10^{-12} \text{ yr}^{-1}$, which corresponds to a mass doubling time of 105 billion years. This is in agreement with the results of the numerical and semi-analytical work (e.g., Bell et al. 2006; De Lucia & Blaizot 2007) that galaxy growth by star formation is not significant at $z < 1$ in BCGs.

Based on their high radio power, the BCGs are AGN-powered radio sources, consistent with expectations for BCGs (Best et al. 2007; Von Der Linden et al. 2007). This is consistent with the AGN and star formation in these sources both being fueled by cold gas in the host galaxy.

We thank the referee for constructive comments which helped make this paper a more robust study. We would like to thank the referee for constructive comments which helped make this paper a more robust study. We thank Kevin Fogarty of Johns Hopkins University for his advice on the nature of old stars in the UV and his UV model of SFR-poor elliptical satellites. We thank Elisabete Da Cunha for her upper-limit-capable MAGPHYS code as well as her advice in its implementation. GRT acknowledges support from the NASA through Einstein Postdoctoral Fellowship Award Number PF-150128, issued by the Chandra X-ray Observatory Center, which is operated by the Smithsonian Astrophysical Observatory for and on behalf of NASA under contract NAS8-03060. Funding for SDSS-III has been provided by the Alfred P. Sloan Foundation, the Participating Institutions, the National Science Foundation, and the U.S. Department of Energy Office of Science. The SDSS-III web site is <http://www.sdss3.org/>. SDSS-III is managed by the Astrophysical Research Consortium for the Participating Institutions of the SDSS-III Collaboration including the University of Arizona, the Brazilian Participation Group, Brookhaven National Laboratory, Carnegie Mellon University, University of Florida, the French Participation Group, the German Participation Group, Harvard University, the Instituto de Astrofísica de Canarias, the Michigan State/Notre Dame/JINA Participation Group, Johns Hopkins University, Lawrence Berkeley National Laboratory, Max Planck Institute for Astrophysics, Max Planck Institute for Extraterrestrial Physics, New Mexico State University, New York University, Ohio State University, Pennsylvania State University, University of Portsmouth, Princeton University, the Spanish Participation Group, University of Tokyo, University of Utah, Vanderbilt University, University of Virginia, University of Washington, and Yale University. Based on observations made with the NASA *Galaxy Evolution Explorer*. GALEX is operated for NASA by the California Institute of Technology under NASA contract NAS5-98034. Based on observations made with the NASA/ESA *Hubble Space Telescope*, obtained from the Data Archive at the

Space Telescope Science Institute, which is operated by the Association of Universities for Research in Astronomy, Inc., under NASA contract NAS 5-26555. These observations are associated with program #13003. This publication makes use of data products from the *Wide-field Infrared Survey Explorer*, which is a joint project of the University of California, Los Angeles, and the Jet Propulsion Laboratory/California Institute of Technology, funded by the National Aeronautics and Space Administration. *Herschel* is an ESA space observatory with science instruments provided by European-led Principal Investigator consortia and with important participation from NASA. HCSS / HSpot / HIPE is a joint development (are joint developments) by the Herschel Science Ground Segment Consortium, consisting of ESA, the NASA Herschel Science Center, and the HIFI, PACS, and SPIRE consortia. The National Radio Astronomy Observatory is a facility of the National Science Foundation operated under cooperative agreement by Associated Universities, Inc.

REFERENCES

- Ahn, C. P., Alexandroff, R., Allende Prieto, C., et al. 2012, *ApJS*, 203, 21
- Alam, S., Albareti, F. D., Allende Prieto, C., et al. 2015, *ApJS*, 219, 12
- Allen, S. W., Rapetti, D. A., Schmidt, R. W., et al. 2008, *MNRAS*, 383, 879
- Ascaso, B., Lemaux, B. C., Lubin, L. M., et al. 2014, *MNRAS*, 442, 589
- Auriemma, C., Perola, G. C., Ekers, R. D., et al. 1977, *A&A*, 57, 41
- Bayliss, M. B., Hennawi, J. F., Gladders, M. D., et al. 2011, *ApJS*, 193, 27
- Bell, E. F., Naab, T., McIntosh, D. H., et al. 2006, *ApJ*, 640, 241
- Bernardi, M. 2009, *MNRAS*, 395, 1491
- Bernardi, M., Hyde, J. B., Sheth, R. K., Miller, C. J., & Nichol, R. C. 2007, *AJ*, 133, 1741
- Best, P. N., & Heckman, T. M. 2012, *MNRAS*, 421, 1569
- Best, P. N., Kauffmann, G., Heckman, T. M., et al. 2005, *MNRAS*, 362, 25
- Best, P. N., von der Linden, A., Kauffmann, G., Heckman, T. M., & Kaiser, C. R. 2007, *MNRAS*, 379, 894
- Blanton, M. R., Dalcanton, J., Eisenstein, D., et al. 2001, *AJ*, 121, 2358
- Bridle, A. H. 1984, *AJ*, 89, 979
- Brinchmann, J., Charlot, S., White, S. D. M., et al. 2004, *MNRAS*, 351, 1151
- Brough, S., Collins, C. A., Burke, D. J., Lynam, P. D., & Mann, R. G. 2005, *MNRAS*, 364, 1354
- Brown, M. J. I., Jannuzi, B. T., Floyd, D. J. E., & Mould, J. R. 2011, *ApJ*, 731, L41
- Bruzual, G. 2007, in *Astronomical Society of the Pacific Conference Series*, Vol. 374, *From Stars to Galaxies: Building the Pieces to Build Up the Universe*, ed. A. Vallenari, R. Tantalo, L. Portinari, & A. Moretti, 303
- Bruzual, G., & Charlot, S. 2003, *MNRAS*, 344, 1000
- Burke, C., & Collins, C. A. 2013, *MNRAS*, 434, 2856
- Burke, C., Hilton, M., & Collins, C. 2015, *MNRAS*, arXiv:1503.04321v1
- Cantalupo, C. M., Borriell, J. D., Jaffe, A. H., Kisner, T. S., & Stomp, R. 2010, *ApJS*, 187, 212
- Carollo, C. M., Bschorr, T. J., Renzini, A., et al. 2013, *ApJ*, 773, 112
- Cavagnolo, K. W., McNamara, B. R., Nulsen, P. E. J., et al. 2010, *ApJ*, 720, 1066
- Collins, C. A., Stott, J. P., Hilton, M., et al. 2009, *Nature*, 458, 603
- Condon, J. 1992, *ARA&A*, 30, 575
- Condon, J., Cotton, W., Greisen, E., et al. 1998, *AJ*, 115, 1693
- Crawford, C. S., Allen, S. W., Ebeling, H., Edge, A. C., & Fabian, A. C. 1999, *MNRAS*, 306, 857
- Cutri, R. M., & et al. 2013, *VizieR Online Data Catalog*, 2328, 0
- da Cunha, E., Charlot, S., & Elbaz, D. 2008, *MNRAS*, 388, 1595
- Daddi, E., Dickinson, M., Morrison, G., et al. 2007, *ApJ*, 670, 156
- Daly, R. A., Sprinkle, T. B., O’Dea, C. P., Kharb, P., & Baum, S. A. 2012, *MNRAS*, 423, 2498
- De Lucia, G., & Blaizot, J. 2007, *MNRAS*, 375, 2

- De Lucia, G., Springel, V., White, S. D. M., Croton, D., & Kauffmann, G. 2006, *MNRAS*, 366, 499
- Donahue, M., Bruch, S., Wang, E., et al. 2010, *ApJ*, 715, 881
- Donahue, M., Connor, T., Fogarty, K., et al. 2015, *ApJ*, 805, 177
- Dressel, L. L. 1981, *ApJ*, 245, 25
- Edwards, L. O. V., Hudson, M. J., Balogh, M. L., & Smith, R. J. 2007, *MNRAS*, 379, 100
- Egami, E., Rex, M., Rawle, T. D., et al. 2010, *A&A*, 518, L12
- Eilek, J. A., & Shore, S. N. 1989, *ApJ*, 342, 187
- Elbaz, D., Daddi, E., Le Borgne, D., et al. 2007, *A&A*, 468, 33
- Fabian, A. C. 1994, *ARA&A*, 32, 277
- , 2012, *ARA&A*, 50, 455
- Fanaroff, B. L., & Riley, J. M. 1974, *MNRAS*, 167, 31P
- Fogarty, K., Postman, M., Connor, T., Donahue, M., & Moustakas, J. 2015, *ApJ*, 813, 117
- Fraser-McKelvie, A., Brown, M. J. I., & Pimblett, K. A. 2014, *MNRAS*, 444, L63
- Gaspari, M., Brighenti, F., & Temi, P. 2015, *A&A*, 579, A62
- Gaspari, M., Ruszkowski, M., & Oh, S. P. 2013, *MNRAS*, 432, 3401
- Giacintucci, S., Markevitch, M., Venturi, T., et al. 2014, *ApJ*, 781, 9
- Gunn, J. E., Siegmund, W. a., Mannery, E. J., et al. 2006, *AJ*, 131, 2332
- Helfand, D. J., White, R. L., & Becker, R. H. 2015, *ApJ*, 801, 26
- Hennawi, J. F., Gladders, M. D., Oguri, M., et al. 2008, *AJ*, 135, 664
- Hicks, A. K., Mushotzky, R., & Donahue, M. 2010, *ApJ*, 719, 1844
- Hlavacek-Larrondo, J., Fabian, A. C., Edge, A. C., & Hogan, M. T. 2012, *MNRAS*, 424, 224
- Hlavacek-Larrondo, J., Allen, S. W., Taylor, G. B., et al. 2013, *ApJ*, 777, 163
- Hopkins, P. F., Hernquist, L., Cox, T. J., Keres, D., & Wuyts, S. 2009, *ApJ*, 691, 1424
- Inagaki, T., Lin, Y.-T., Huang, H.-J., Hsieh, B.-C., & Sugiyama, N. 2015, *MNRAS*, 446, 1107
- Jimenez, R., Bernardi, M., Haiman, Z., Panter, B., & Heavens, A. F. 2007, *ApJ*, 669, 947
- Kennicutt, R. C. 1998, *ARA&A*, 36, 189
- Khochfar, S., & Burkert, A. 2003, *ApJ*, 597, L117
- Lara-López, M. A., Cepa, J., Bongiovanni, A., et al. 2010, *A&A*, 521, L53
- Lauer, T. R., Postman, M., Strauss, M. A., Graves, G. J., & Chisari, N. E. 2014, *ApJ*, 797, 82
- Lauer, T. R., Gebhardt, K., Faber, S. M., et al. 2007, *ApJ*, 664, 226
- Ledlow, M. J., & Owen, F. N. 1996, *AJ*, 112, 9
- Lee, N., Sanders, D. B., Casey, C. M., et al. 2015, *ApJ*, 801, 80
- Li, N., & Thakar, A. R. 2008, *Computing in Science and Engineering*, 10, 18
- Li, Y., & Bryan, G. L. 2014, *ApJ*, 789, 54
- Lidman, C., Suherli, J., Muzzin, A., et al. 2012, *MNRAS*, 427, 550
- Lin, Y.-T., Brodwin, M., Gonzalez, A. H., et al. 2013, *ApJ*, 771, 61
- Lin, Y.-T., & Mohr, J. J. 2004, *ApJ*, 617, 879
- Liu, F. S., Mao, S., & Meng, X. M. 2012, *MNRAS*, 423, 422
- Martin, D. C., Fanson, J., Schiminovich, D., et al. 2005, *ApJ*, 619, L1
- McDonald, M., Stalder, B., Bayliss, M., et al. 2016, *ApJ*, 817, 86
- McMullin, J. P., Waters, B., Schiebel, D., Young, W., & Golap, K. 2007, in *ASP Conf. Ser.*, Vol. 376, *Astronomical Data Analysis Software and Systems XVI*, ed. R. A. Shaw, F. Hill, & C. A. Bell, D. J. 1 (San Francisco), 127
- McNamara, B. R., & Nulsen, P. E. J. 2007, *ARA&A*, 45, 117
- , 2012, *New Journal of Physics*, 14, 055023
- Mittal, R., Whelan, J. T., & Combes, F. 2015, *MNRAS*, 450, 2564
- Morrissey, P., Conrow, T., Barlow, T. A., et al. 2007, *ApJS*, 173, 682
- Noeske, K. G., Faber, S. M., Weiner, B. J., et al. 2007, *ApJ*, 660, L47
- O’Connell, R. W. 1999, *ARA&A*, 37, 603
- O’Dea, C. P., Baum, S. A., Privon, G., et al. 2008, *ApJ*, 681, 1035
- O’Dea, K. P., Quillen, A. C., O’Dea, C. P., et al. 2010, *ApJ*, 719, 1619
- Oguri, M., Bayliss, M. B., Dahle, H. k., et al. 2012, *MNRAS*, 420, 3213
- Petrosian, V. 1976, *ApJ*, 209, L1
- Pilbratt, G. L., Riedinger, J. R., Passvogel, T., et al. 2010, *A&A*, 518, L1
- Pipino, A., Kaviraj, S., Bildfell, C., et al. 2009, *MNRAS*, 395, 462
- Pipino, A., Szabo, T., Pierpaoli, E., MacKenzie, S. M., & Dong, F. 2011, *MNRAS*, 417, 2817
- Pizzolato, F., & Soker, N. 2005, *ApJ*, 632, 821
- Postman, M., Coe, D., Benítez, N., et al. 2012, *ApJS*, 199, 25
- Rhoads, J. E., Malhotra, S., Allam, S., et al. 2014, *ApJ*, 787, 8
- Saglia, R. P., Sánchez-Blázquez, P., Bender, R., et al. 2010, *A&A*, 524, A6
- Saintonge, A., Lutz, D., Genzel, R., et al. 2013, *ApJ*, 778, 2
- Santini, P., Fontana, A., Grazian, A., et al. 2009, *A&A*, 504, 751
- Schlaafy, E. F., & Finkbeiner, D. P. 2011, *ApJ*, 737, 103
- Shankar, F., Buchan, S., Rettura, A., et al. 2015, *ApJ*, 802, 73
- Stott, J. P., Collins, C. A., Burke, C., Hamilton-Morris, V., & Smith, G. P. 2011, *MNRAS*, 414, 445
- Sun, M. 2009, *ApJ*, 704, 1586
- Thomas, D., Maraston, C., Bender, R., & Mendes de Oliveira, C. 2005, *ApJ*, 621, 673
- Thompson, A., Clark, B., Wade, C., & Napier, P. 1980, *ApJS*, 44, 151
- Tremblay, G. R., Gladders, M. D., Baum, S. A., et al. 2014, *ApJ*, 790, L26
- Tremblay, G. R., O’Dea, C. P., Baum, S. A., et al. 2015, *MNRAS*, 451, 3768
- Tremblay, G. R., Oonk, J. B. R., Combes, F., et al. 2016, *Nature*, 534, 218
- Treu, T., Ellis, R. S., Liao, T. X., et al. 2005, *ApJ*, 633, 174
- Vaddi, S., O’Dea, C. P., Baum, S. A., et al. 2016, *ApJ*, 818, 182
- van Dokkum, P. G., & Franx, M. 1996, *MNRAS*, 281, 985
- Von Der Linden, A., Best, P. N., Kauffmann, G., & White, S. D. M. 2007, *MNRAS*, 379, 867
- Vulcani, B., Marchesini, D., De Lucia, G., et al. 2016, *ApJ*, 816, 86
- Wang, J., Overzier, R., Kauffmann, G., Von Der Linden, A., & Kong, X. 2010, *MNRAS*, 401, 433
- Wiley, I. M., Aragón-Salamanca, A., De Lucia, G., et al. 2008, *MNRAS*, 387, 1253
- Wright, E. L., Eisenhardt, P. R. M., Mainzer, A., et al. 2010, *AJ*, 140, 22
- Zahid, H. J., Yates, R. M., Kewley, L. J., & Kudritzki, R. P. 2013, *ApJ*, 763, 92

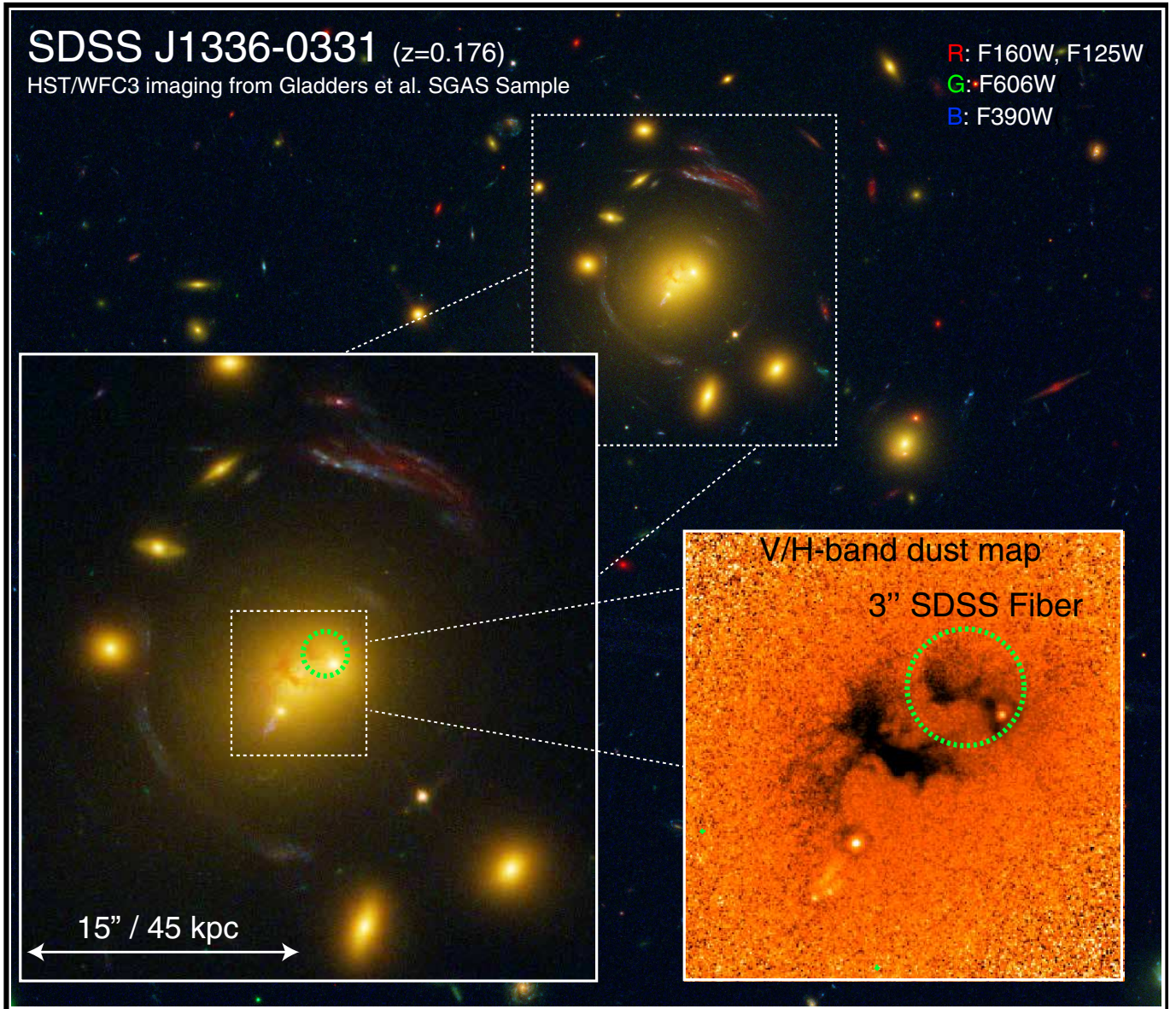


Figure 9. Left: *Hubble Space Telescope* WFC3 three-color composite observation of cluster SDSSJ1336-0331 (PI: Michael D. Gladders, ID: 13003) with an exposure time of 2400 s using filters F390W (blue), F606W (green), and F160W + F125W (red). The green circle indicates the area subtended by the 3'' diameter SDSS spectroscopic fiber. Heavy dust obscuration covers the eastern nucleus, and a radial lensed feature is visible near the southeast. The SDSS fiber misses any star formation in much of the southeast. 3'' subtends 12.4 kpc at the target redshift. Bottom right: V/H-band color map revealing considerable substructure to the north and east along both nuclei.

Table 1
CLASH and SGAS BCG Samples

Target ID	α_{J2000} (degrees)	δ_{J2000} (degrees)	Redshift (z)	Stellar Mass (M_{\odot})	χ^2	Sample
Abell 209	01:31:52.6	-13:36:38.80	0.206	4.85e+11	0.599	CLASH
Abell 383	02:48:03.4	-03:31:44.7	0.187	4.45e+11	5.331	CLASH
Abell 611	08:00:56.8	+36:03:24.1	0.288	6.58e+11	146.998	CLASH
Abell 1423	11:57:17.3	+33:36:37.4	0.213	4.83e+11	3.308	CLASH
Abell 2261	17:22:27.2	+32:07:58.6	0.224	1.23e+12	12.845	CLASH
CLJ1226.9+3332	12:26:58.4	+33:32:47.4	0.89	1.21e+12	5.748	CLASH
MACS0329.7-0211	03:29:41.7	-02:11:47.7	0.45	8.47e+11	0.235	CLASH
MACS0416.1-2403	04:16:09.4	-24:04:03.9	0.42	3.14e+11	0.452	CLASH
MACS0429.6-0253	04:29:36.1	-02:53:08.0	0.399	1.19e+12	0.004	CLASH
MACS0647.8+7015	06:47:50.0	+70:14:49.7	0.584	1.47e+12	0.054	CLASH
MACS0710.5+3745	07:17:31.7	+37:45:18.5	0.548	2.19e+11	0.015	CLASH
MACS0744.9+3927	07:44:52.8	+39:27:24.4	0.686	7.74e+11	1.175	CLASH
MACS1115.9+0129	11:15:52.1	+01:29:56.6	0.352	3e+11	2.1	CLASH
MACS1149.6+2223	11:49:35.9	+22:23:55.0	0.544	4.72e+11	1.907	CLASH
MACS1206.2-0847	12:06:12.3	-08:48:02.4	0.44	3.13e+11	1.129	CLASH
MACS1211.0-0210	13:11:01.7	-03:10:39.5	0.494	3.69e+11	1.068	CLASH
MACS1423.8+2404	14:23:47.8	+24:04:40.5	0.545	5.65e+11	1.145	CLASH
MACS1720.3+3536	17:20:17.0	+35:36:23.6	0.391	6.59e+11	11.689	CLASH
MACS1931.8-2635	19:31:49.7	-26:34:34.0	0.352	6.92e+11	12.782	CLASH
MACS2129.4-0741	21:29:26.1	-07:41:28.8	0.57	9.37e+11	8.04	CLASH
MS2137-2353	21:40:15.2	-23:39:40.7	0.313	3.65e+11	0.242	CLASH
RXJ1347.5-1145	13:47:30.6	-11:45:10.1	0.451	4.52e+11	0.026	CLASH
RXJ1532.9+3021	15:32:53.8	+30:20:58.7	0.345	3.34e+11	12.048	CLASH
RXJ2129.7+0005	21:29:39.9	+00:05:18.8	0.234	5.81e+11	3.317	CLASH
RXJ2248.7-4431	22:48:44.3	-44:31:48.4	0.348	8.09e+11	0.065	CLASH
SDSSJ0004-0103	00:04:51.9	-01:03:15.80	0.479	5.31e+11	0.941	SGAS
SDSSJ0108+0624	01:08:42.0	+06:24:43.50	0.549	1.67e+11	4.877	SGAS
SDSSJ0146-0929	01:46:56.0	-09:29:52.40	0.447	9.74e+11	1.036	SGAS
SDSSJ0150+2725	01:50:00.9	+27:25:36.20	0.3	1.22e+12	171.751	SGAS
SDSSJ0851+3331	08:51:39.0	+33:31:10.83	0.371	6.5e+11	2.036	SGAS
SDSSJ0915+3826	09:15:39.0	+38:26:58.77	0.396	...	999.0	SGAS
SDSSJ0928+2031	09:28:05.6	+20:31:25.55	0.192	...	999.0	SGAS
SDSSJ0952+3434	09:52:40.0	+34:34:47.09	0.359	4.08e+11	3.055	SGAS
SDSSJ0957+0509	09:57:39.2	+05:09:31.80	0.447	5.22e+11	0.283	SGAS
SDSSJ1002+2031	10:02:26.9	+20:31:02.61	0.321	4.91e+11	0.358	SGAS
SDSSJ1038+4849	10:38:43.2	+48:49:18.73	0.432	2.61e+12	8.098	SGAS
SDSSJ1050+0017	10:50:39.9	+00:17:06.91	0.3	7.87e+11	3.303	SGAS
SDSSJ1055+5547	10:55:04.6	+55:48:23.23	0.462	7.59e+11	2.304	SGAS
SDSSJ1110+6459	11:10:17.6	+64:59:47.02	0.659	3.9e+11	1.592	SGAS
SDSSJ1115+1645	11:15:04.4	+16:45:38.40	0.191	2.81e+11	2.971	SGAS
SDSSJ1138+2754	11:38:09.0	+27:54:30.90	0.454	1.91e+11	0.221	SGAS
SDSSJ1152+0930	11:52:47.3	+09:30:14.54	0.521	8.23e+11	0.537	SGAS
SDSSJ1152+3313	11:52:00.3	+33:13:41.72	0.357	8.17e+11	2.322	SGAS
SDSSJ1156+1911	11:56:05.5	+19:11:12.68	0.546	6.14e+11	0.314	SGAS
SDSSJ1207+5254	12:07:36.4	+52:54:58.20	0.273	7.89e+11	9.278	SGAS
SDSSJ1209+2640	12:09:23.7	+26:40:46.50	0.559	8.02e+11	2.811	SGAS
SDSSJ1329+2243	13:29:34.5	+22:43:00.24	0.42	2.57e+12	89.54	SGAS
SDSSJ1336-0331	13:36:00.0	-03:31:28.63	0.176	6.94e+11	53.666	SGAS
SDSSJ1343+4155	13:43:32.8	+41:55:04.48	0.418	6.46e+11	41.59	SGAS
SDSSJ1439+1208	14:39:09.9	+12:08:24.75	0.427	3.24e+11	0.735	SGAS
SDSSJ1456+5702	14:56:00.8	+57:02:20.60	0.483	8.31e+11	0.672	SGAS
SDSSJ1527+0652	15:27:45.4	+06:52:31.79	0.394	4.84e+11	0.6	SGAS
SDSSJ1531+3414	15:31:10.6	+34:14:24.91	0.335	3.05e+11	0.477	SGAS
SDSSJ1604+2244	16:04:10.2	+22:44:16.69	0.281	3.46e+11	1.368	SGAS
SDSSJ1632+3500	16:32:10.3	+35:00:30.16	0.475	9.04e+11	0.511	SGAS
SDSSJ1723+3411	17:23:36.2	+34:11:59.37	0.442	5.39e+11	0.487	SGAS
SDSSJ2111-0114	21:11:19.4	-01:14:23.57	0.639	3.72e+12	12.035	SGAS

References. — da Cunha et al. (2008), Postman et al. (2012), M.D. Gladders et al. in preparation

Note. — Columns: Target, R.A.(J2000), Decl.(J2000), SDSS redshift, MAGPHYS estimated stellar mass (M_{\odot}), fit χ^2 , and original subsample. * denotes that RXJ2248.7-4431 is alternately named Abell 1063S.

Table 2
CLASH and SGAS BCG Star Formation Rate Estimators

Target ID	NUV SFR ($M_{\odot}\text{yr}^{-1}$)	NUV SFR Error ($M_{\odot}\text{yr}^{-1}$)	NUV Quality	H α SFR ($M_{\odot}\text{yr}^{-1}$)	H α SFR Error ($M_{\odot}\text{yr}^{-1}$)	[O II] SFR ($M_{\odot}\text{yr}^{-1}$)	[O II] SFR Error ($M_{\odot}\text{yr}^{-1}$)
Abell 209	1.85	0.13	D
Abell 383	5.74	1.08	D
Abell 611	N	0.06	0.10
Abell 1423	N
Abell 2261	N	0.09	0.07	0.01	0.04
CLJ1226.9+3332	1.85	0.402	L
MACS0329.7-0211	13.20	0.92	D
MACS0416.1-2403	3.11	0.80	L
MACS0429.6-0253	N
MACS0647.8+7015	N
MACS0710.5+3745	N
MACS0744.9+3927	N	0.41	0.12
MACS1115.9+0129	5.38	0.59	D	2.83	0.19	3.91	0.37
MACS1149.6+2223	4.74	2.04	L
MACS1206.2-0847	N
MACS1211.0-0210	N
MACS1423.8+2404	7.6	1.47	D
MACS1720.3+3536	N
MACS1931.8-2635	49.51	4.72	D
MACS2129.4-0741	4.74	2.32	L
MS2137-2353	2.21	0.09	L
RXJ1347.5-1145	7.55	0.44	D
RXJ1532.9+3021	N	31.88	0.38	43.53	1.36
RXJ2129.7+0005	1.71	0.64	D	1.71	0.05	2.81	0.19
RXJ2248.7-4431	N
SDSSJ0004-0103	1.33	0.37	L
SDSSJ0108+0624	N
SDSSJ0146-0929	N	0.09	0.03
SDSSJ0150+2725	2.54	1.04	L
SDSSJ0851+3331	0.19	0.42	L
SDSSJ0915+3826	1.91	0.55	L	0.28	0.127	0.03	1.02
SDSSJ0928+2031	0.17	0.06	L	0.16	0.08
SDSSJ0952+3434	1.72	0.67	L	0.55	0.039
SDSSJ0957+0509	N
SDSSJ1002+2031	N	0.03	0.04
SDSSJ1038+4849	7.6	2.04	L	0.14	0.25
SDSSJ1050+0017	0.7	0.28	L
SDSSJ1055+5547	N	1.51	1.92
SDSSJ1110+6459	N
SDSSJ1115+1645	0.25	0.18	L	0.04	0.01	0.04	0.17
SDSSJ1138+2754	8.22	2.76	L
SDSSJ1152+0930	N	0.13	0.42
SDSSJ1152+3313	N	0.10	0.10	0.14	0.19
SDSSJ1156+1911	3.44	1.37	L
SDSSJ1207+5254	0.28	0.13	L	0.20	0.10	0.07	0.07
SDSSJ1209+2640	N	0.11	1.50
SDSSJ1329+2243	0.99	0.31	L
SDSSJ1336-0331	3.76	1.473	D	1.83	0.53
SDSSJ1343+4155	N
SDSSJ1439+1208	N	0.30	1.35
SDSSJ1456+5702	N	0.13	0.29
SDSSJ1527+0652	2.23	1.085	L
SDSSJ1531+3414	N	1.60	0.44	1.94	1.01
SDSSJ1604+2244	N	0.07	0.11
SDSSJ1632+3500	0.76	0.43	L
SDSSJ1723+3411	N
SDSSJ2111-0114	N

Note. — Columns: Target ID, NUV star formation rate and error; NUV data quality (N - no data, L - 95% Confidence Upper Limit, D-detection); H α SFR and error; and [O II] SFR and error. All star formation rates are in units of $M_{\odot}\text{yr}$ and errors represent 1σ values.